# Wave Interaction of Reverse-Fault Rupture with Free Surface: Numerical Analysis of the Dynamic Effects and Fault Opening Induced by Symmetry Breaking.

**A. Scala[1,2], G. Festa[1], J.-P. Vilotte[3], S. Lorito[2], F. Romano[2]**

[1]Dipartimento di Fisica "Ettore Pancini" – Università degli studi di Napoli Federico II, Italy
[2]Istituto Nazionale di Geofisica e Vulcanologia (INGV) – Sezione Roma 1, Italy.
[3]Institut de Physique du Globe de Paris, CNRS-INSU, France
Corresponding author: Antonio Scala (antonio.scala@ingv.it)

**Key Points:**

- Symmetry breaking from free surface/rupture interaction may enhance slip, ground motion, tsunamigenic potential of shallow ruptures.
- Rupture dynamics deviates from classical linear elastic fracture mechanics: inertial effects in the energy balance and shallow opening.
- The effects of the interaction are strongly sensitive to the friction level; the higher the friction, the more important the interaction.

# Abstract

Several great earthquakes occur on thrust faults both along subduction and continental collision zones. These events often feature a large shallow slip patch, and an asymmetric pattern for the ground motion and the static deformation between the hanging-wall and the footwall of the fault.

From a mechanical point of view, this asymmetry can be partially explained taking into account the interaction between the fault and the seismic radiation emitted during rupture propagation and stored in the hanging-wall in the vicinity of the free surface.

We numerically investigate the rupture dynamics along a thrust dipping fault impacting onto the free surface at a dip angle of $\delta = 20°$, in a 2D elastic model.

We show how the wave interaction of the rupture with the free surface leads to a breaking of the reflection symmetry. Compared to a rupture propagating in an infinite medium, this interaction enhances the slip rate in the up-dip direction as an effect of the coupling between slip and normal traction around the crack front.

The breaking of symmetry leads to sizeable acceleration of the rupture toward asymptotic speed with inertia acquisition, dependence of the rupture dynamics on the level of friction along the interface and might produce an interface opening over a finite length in the vicinity of the surface. We finally explore how the wave interaction drives amplification and asymmetry of the shallow slip and the vertical displacement at the surface.

The described effects should be considered in various numerical approaches and in interpretation of geophysical observations.

# 1. Introduction

Understanding the dynamics of a spontaneously propagating frictional rupture along a thrust fault embedded in elastic media is a long-standing problem with important theoretical and practical implications in the context of active collision and subduction zones, where large earthquakes predominantly occur.

Noteworthy observations associated with these earthquakes show large shallow slip and/or an asymmetric ground motion in the hanging wall in the vicinity of the fault - with much larger strong motion and possibly inelastic deformation - that may trigger significant structural damage, and/or destructive tsunamis, such as for the 1994, Mw 6.7, Northridge earthquake (Abrahamson & Summerville 1996), the 1999, Mw 7.7, Chi-Chi earthquake (Zhang et al., 2008), the 2004, Mw 9.2, Sumatra earthquake (Shearer & Burgmann 2010), the 2011, Mw 9.1, Tohoku earthquake (Satake et al., 2013; Lay 2018), and the 2013, Mw 7.7, Balochistan earthquake (Vallage et al., 2015).

Numerical investigations (Nielsen 1998; Oglesby et al., 1998, 2000; Ma & Archuleta 2006; Uenishi 2015; Murphy et al., 2016) of spontaneous rupture propagation along a thrust fault separating two identical elastic materials have shown that slip-induced normal traction variations and interaction of the rupture with the free-surface through seismic waves enhance the rupture propagation in the up-dip direction with large slip close to the surface. This wave interaction also enhances the amount of radiated energy along the forward rupture direction and with an asymmetry in the ground-motion and the surface deformation (Brune 1996). This has been interpreted as resulting from trapped waves in the hanging wall together with a geometrically induced effective compliance of the hanging wall. Material asymmetry between the hanging-wall and the footwall has also been numerically investigated (Ma & Beroza, 2008; Kozdon & Dunham 2013; Lotto et al., 2017), in particular in the context of subduction zones. Directivity of the rupture propagation induced by the bimaterial interface is shown to further favour the up-dip rupture propagation and to allow the penetration of the rupture also in velocity strengthening shallow portions of the frictional interface close to the surface. The bimaterial effect increases the strength drop along the interface, together with the ground motion

67 asymmetry and slip concentration close to the surface. However, when a dynamically induced
68 inelastic effect is included in the hanging wall (Ma 2012; Ma & Hirakawa 2013), lower radiated
69 energy and rupture velocity, together with a smaller directivity effect are predicted as observed for
70 shallow subduction earthquakes.
71 Laboratory thrust-fault experiments combined with linear elastic numerical simulations (e.g. Brune
72 1996; Shi et al. 1998) have also provided further insights on the implication of geometrical and
73 material symmetry breaking on subshear and supershear rupture propagation. In particular,
74 experiments and numerical simulations of Gabuchian et al. (2014, 2017) reveal the existence of a
75 geometrically induced torque mechanism in the hanging-wall. This mechanism reduces the normal
76 traction along the shallow portion of the interface. The weakening of the interface promotes dynamic
77 rupture propagation up to the surface where spontaneous fault opening can be triggered. At this stage,
78 a supershear propagation of the rupture down-dip is nucleated, trailed by a sliding pulse propagating
79 at Rayleigh wave speed. Fault opening is supported by early linear elastic fracture mechanics analysis
80 (Erdogan & Arin 1975; Rudnicki & Wu 1995; Brune 1996).
81 In a different context, recent analytic linear stability analysis (Aldam et al., 2016, Brener et al., 2016)
82 shows that geometrical symmetry breaking and interaction with the domain boundary have an
83 important implication on the stability of a finite-height elastic layer sliding atop of a semi-infinite
84 elastic half-space along a velocity-strengthening frictional interface. The sliding stability is controlled
85 by slip-induced normal traction variations and by the absolute level of friction along the interface,
86 both of which depend on the degree of geometrical asymmetry. These studies provide new insights
87 on the implication of symmetry breaking on the rupture dynamics when the rupture interacts with
88 boundaries.
89 Finally, laboratory experiments (Goldman et al. 2010; Fineberg & Bouchinder 2015), and analytical
90 studies (Marder 1991; Zhou & Shioya 1996) have shed a light on interactions of reflected waves with
91 the rupture when the system has a reflection symmetry across the interface. For a rupture propagating
92 in a long elastic strip, effective inertial dynamics are inherited from the interaction of the rupture with

93 the strip boundaries, mediated by the waves radiated during the rupture and reflected at the boundary,
94 giving rise to an acceleration-dependent energy release rate (with a velocity-dependent effective
95 mass) and a memory effect. This is in contrast with a rupture propagating in an infinite medium for
96 which rupture front dynamics are not inertial, i.e., the rupture front behaves as a massless particle
97 where acceleration plays no role. When rupture interacts with boundaries, effective inertia dynamics
98 control the rupture acceleration toward the asymptotic propagation speed.
99 Spontaneous rupture dynamics along reverse-fault frictional interface is thus a not yet well
100 understood complex problem. The effect of the interaction between rupture and waves generated at
101 the free surface depends on the specific wave type and on the dynamic stage of the rupture at the time
102 of the interaction. The lack of symmetry, even when the interface separates two identical materials,
103 leads to a coupling between the interfacial slip and the normal traction variations with implications
104 on the rupture dynamics and directivity, such as memory and inertial effects, opening and a
105 dependence on the frictional level, that need to be finely addressed.
106 In this paper, we use extensive numerical simulations to address spontaneous dynamic rupture
107 propagation along a slip-weakening frictional interface separating two identical elastic materials. The
108 goal is to explore the implications of the geometric symmetry breaking and of the interaction between
109 the rupture and seismic waves generated at the free surface on the rupture dynamics and the induced
110 surface deformation. This is done through a systematic numerical comparison with a symmetric fault
111 interface. Specifically, we finely analyse sliding-induced normal traction variations during the
112 spontaneous rupture propagation due to reflected body and Rayleigh waves from the free surface and
113 their effect on the rupture dynamics. We then investigate effective inertial dynamics occurring during
114 the rupture acceleration toward the asymptotic speed and explore the opening effect near the surface
115 and the influence of the absolute frictional level on the energy release rate under the condition of
116 symmetry breaking.
117 The paper is organised as follows. The numerical method and the geometrical setup of the simulations
118 are described in section 2; the results are presented in section 3 through systematic comparisons

between the free surface and the unbounded medium cases, for different nucleation depths and different levels of friction.

# 2. Numerical method and setup

## 2.1. Mechanical method

We numerically solve the elastodynamic equation in each point $\mathbf{x}$ of the elastic domain and for each time $t$ to describe the propagation of seismic waves in an elastic medium:

$$\begin{cases} \boldsymbol{\rho}(\mathbf{x})\dot{\mathbf{v}}(\mathbf{x},\boldsymbol{t}) = \vec{\boldsymbol{\nabla}} \cdot \boldsymbol{\sigma}(\mathbf{x},\boldsymbol{t}) \\ \dot{\boldsymbol{\sigma}}(\mathbf{x},\boldsymbol{t}) = \mathbf{c}(\mathbf{x}) : \vec{\boldsymbol{\nabla}}\mathbf{v}(\mathbf{x},\boldsymbol{t}) \end{cases} \quad (1)$$

Here $\rho(\mathbf{x})$ is the material density, $\mathbf{v}(\mathbf{x},t)$ is the particle velocity, $\boldsymbol{\sigma}(\mathbf{x},t)$ is the Cauchy stress tensor, and $\mathbf{c}(\mathbf{x})$ is the fourth-order Hooke's tensor for linear elasticity. The dot denotes time derivative. We impose that the traction $\mathbf{T} = \boldsymbol{\sigma} \cdot \mathbf{n}$ is zero at the free surface, where $\mathbf{n}$ is the outward normal to the free surface. We apply contact and friction conditions at the zero-thickness interface representing the fault to dynamically model the rupture propagation. The traction $\mathbf{T}$ is imposed to be continuous across the interface whereas the kinematic quantities can be discontinuous. Slip and slip rate are computed through a domain decomposition along the interface separating the two sub-domains on the two sides of the fault interface, hereinafter referred by the subscripts 1 and 2. We then separately solve the eq. (1) for the two sub-domains. For a point $\boldsymbol{\xi}$ on the interface, we define the interfacial slip and slip rate as $\delta\mathbf{u}(\boldsymbol{\xi},t) = \mathbf{u_2}(\boldsymbol{\xi},t) - \mathbf{u_1}(\boldsymbol{\xi},t)$ and $\delta\mathbf{v}(\boldsymbol{\xi},t) = \mathbf{v_2}(\boldsymbol{\xi},t) - \mathbf{v_1}(\boldsymbol{\xi},t)$ respectively.

We assume a Signorini contact condition along the interface:

$$\begin{cases} \delta u^n(\boldsymbol{\xi},t) \geq 0 \\ T^n(\boldsymbol{\xi},t) \leq 0 \\ \delta u^n(\boldsymbol{\xi},t) \cdot T^n(\boldsymbol{\xi},t) 0 \end{cases} \quad (2)$$

where the superscript $n$ refers to the component of the fields normal to the interface. The normal vector is defined as the outward normal to the fault side belonging to the medium 1. According to the

eq. (2), when the total normal traction is compressive the two blocks are in contact, whereas when the normal traction perturbation is equal to the initial compressive normal traction (total normal traction $T^n = 0$) the interface behaves as a free surface; in this case the two lips of the fault are allowed to separate from each other and a local opening of the interface occurs.

When the two sides of the interface are in contact, the frictional sliding is modelled by imposing the Coulomb condition

$$\begin{cases} (|\mathbf{T}^t(\boldsymbol{\xi},t)| - C(\boldsymbol{\xi}) + \mu \mathrm{T}^n(\boldsymbol{\xi},t)) \cdot |\boldsymbol{\delta}\mathbf{v}^t(\boldsymbol{\xi},t)| = 0 \\ \left(\left||\mathbf{T}^t(\boldsymbol{\xi},t)| - C(\boldsymbol{\xi})\right| + \mu \mathrm{T}^n(\boldsymbol{\xi},t)\right) \leq 0 \\ \mathbf{T}^t(\boldsymbol{\xi},t) \cdot \boldsymbol{\delta}\mathbf{v}^t(\boldsymbol{\xi},t) = |\mathbf{T}^t(\boldsymbol{\xi},t)||\boldsymbol{\delta}\mathbf{v}^t(\boldsymbol{\xi},t)| \end{cases} \quad (3)$$

The superscript $t$ now represent the tangential direction with respect to the interface and $C$ is the cohesion of the interface, which goes to zero at the free surface. We assume a linear slip weakening behaviour of the friction coefficient $\mu$ during the sliding; it linearly decreases from a static level $\mu_s$ to the dynamic one $\mu_d$ over a characteristic slip distance $D_c$; beyond $D_c$ the friction is maintained constant to the dynamic level (Ida 1972). Finally $-\mu(\boldsymbol{\delta}\mathbf{u}^t)\mathrm{T}^n$ is the frictional strength.

First condition in (3) indicates that the frictional sliding ($\left|\delta \mathbf{v}^t\right| \neq 0$) occurs when the tangential traction lies on the surface of the Coulomb cone ($|\mathbf{T}^t| - C + \mu \mathrm{T}^n) = 0$; when the interface is stick, the traction is inside the Coulomb cone (second equation in (3)). The final condition describes the co-linearity between the tangential traction and the slip rate, which is automatically insured in the 2D models presented in this work.

Physical quantities are normalized to provide a general framework for the results. In particular, the slip is normalized by the critical slip weakening distance $\delta\tilde{\mathbf{u}} = \delta\mathbf{u}/D_c$. The traction $\mathbf{T}$ is normalized as $\tilde{\mathbf{T}} = \mathbf{T}/\Delta\sigma_0$ assuming a reference stress drop $\Delta\sigma_0$ as the maximum value of the initial stress drop on the fault, that is $\max[\tau_0(x) - \mu_d \cdot \sigma_n^0(x)]$ with $\tau_0, \mu_d$ and $\sigma_n^0$ being the initial shear traction the dynamic friction coefficient and the initial normal traction respectively. The distance $z$ and the time $t$ are normalized as $\tilde{\mathrm{z}} = \frac{\Delta\sigma_0}{G \cdot D_c}\mathrm{z}$, and $\tilde{t} = \frac{V_s \cdot \Delta\sigma_0}{G \cdot D_c} t$ resepctively, where $G$ is the shear modulus and $V_s$ is

the S-wave velocity. Accordingly, all the rupture and wave speeds are normalized by the S-wave velocity, and the dimensionless slip-rate is derived by the normalization of slip and time.

## 2.2. Geometrical setup and numerical model

We numerically model the fault as a planar interface intersecting the free surface with a dip angle of 20° (Figure 1a); the rupture is nucleated at different depths (red stars in Error! Reference source not found.a-b) and propagates under different absolute levels of friction along the interface.

The numerical approximation is based on the spectral element method (Komatitsch and Vilotte 1998) accounting for non-smooth contact and friction conditions (Festa and Vilotte 2006; Scala et al. 2017). The spatial approximation is based on an irregular quadrangular element mesh. The elements naturally follow the shape of the wedge between the free surface and the shallow part of the fault (Fig S1 in the Supporting Information) without generating any mesh-related artefact. We use $9 \times 9$ Gauss-Lobatto-Legendre collocation points within each element and the size of the elements is chosen to ensure at least 5 points for the minimum wavelength during the rupture propagation (Komatitsch and Vilotte 1998) and 4 points in the process zone.

The time integration is performed through a second-order forward scheme. The stability of the time scheme is ensured by a Courant number of about 0.04.

To numerically mimic an infinite half-space, perfectly matched layers (PMLs) are used on the three other edges of the model (Festa and Vilotte, 2005; Festa et al. 2005); this allows to strongly reduce spurious reflections from the boundaries of the numerical domain. We evaluate the effect of the interaction between the rupture and the free surface through additional numerical simulations performed in an infinite unbounded medium with the same fault geometry, where the free surface is replaced by a PML (Figure 1b). We verified that the fault is far enough from the PMLs avoiding any mesh-dependent numerical artefacts.

## 2.3. Initial conditions

The interface normal traction is imposed to monotonically increase with depth along the dipping fault interface to mimic the lithostatic loading as in similar studies (Huang et al. 2012).

The linear slip weakening friction parameters, that is the static ($\mu_s$) and the dynamic ($\mu_d$) friction coefficients, and the initial strength excess parameter $s = (\mu_s T_0^n - T_0^t)/(T_0^t - \mu_d T_0^n)$ are assumed to be uniform along the interface. In the above formula the subscript 0 refers to the initial value of the field.

As such, the shear traction, the initial stress and strength drop also increase with depth with the maximum stress drop at the bottom of the interface. An interface cohesion $C$ is imposed at about 10% of the maximum stress drop and goes to zero at the free surface.

To analyse the implication of frictional level on the rupture dynamics, and on its interaction with the waves reflected by the surface, different sets of friction values have been investigated. However, the same initial normal traction profile is imposed independently of the friction level. We thus rescale the initial shear traction and we impose for all simulations $\mu_s - \mu_d = 0.2$ in order to keep the same stress drop and strength excess for all the simulations.

The initial traction and interfacial strength initial distributions are illustrated Figure 2, for an initial interface strength-excess *s*=2, and two different sets of static and dynamic friction levels: $\mu_s = 0.60$ - $\mu_d = 0.40$ and $\mu_s = 0.25$ - $\mu_d = 0$. For a strength-excess parameter $s = 2$ an infinite symmetric rupture is not expected to accelerate at super-shear speeds (Burridge 1973).

The rupture is initiated by imposing the initial tangential traction slightly above the frictional strength over a finite length $L_c$, large enough to ensure the dynamic propagation of the rupture away from the nucleation (Uenishi & Rice 2003; Scala et al., 2017).

Different nucleation depths were investigated (See Figure 1). Indeed, depending on the nucleation depth, the interaction can be triggered when the rupture is still in its acceleration phase or it has already reached the asymptotic speed. This aspect may control the acceleration and the stationary propagation of the crack. Moreover, the memory effects inherited from the history of the radiation

might play a role in controlling the rupture dynamics affecting the total stored energy in the hanging-wall.

For a fixed nucleation depth, the ratio $T^t_{Nuc}/T^n$, with $T^t_{Nuc}$ the tangential traction in the nucleation patch, is rescaled in order to keep constant the strength drop in the nucleation area when changing the friction coefficients.

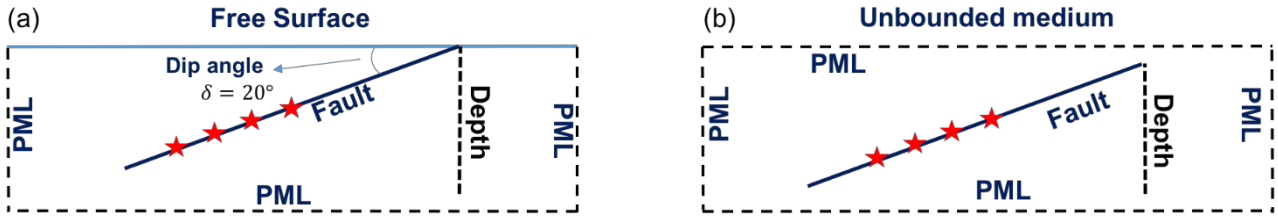


**Figure 1 Geometrical setup for the numerical simulations. Panel (a): a thrust planar fault impacts the the free surface with a dip angle $\delta = 20°$. On the other three boundaries Perfectly Matching Layers (PML) conditions are imposed. The red stars on the fault depict the different nucleation depths. In the panel (b) the same fault is embedded in an infinite medium, obtained surrounding the domain with PMLs.**

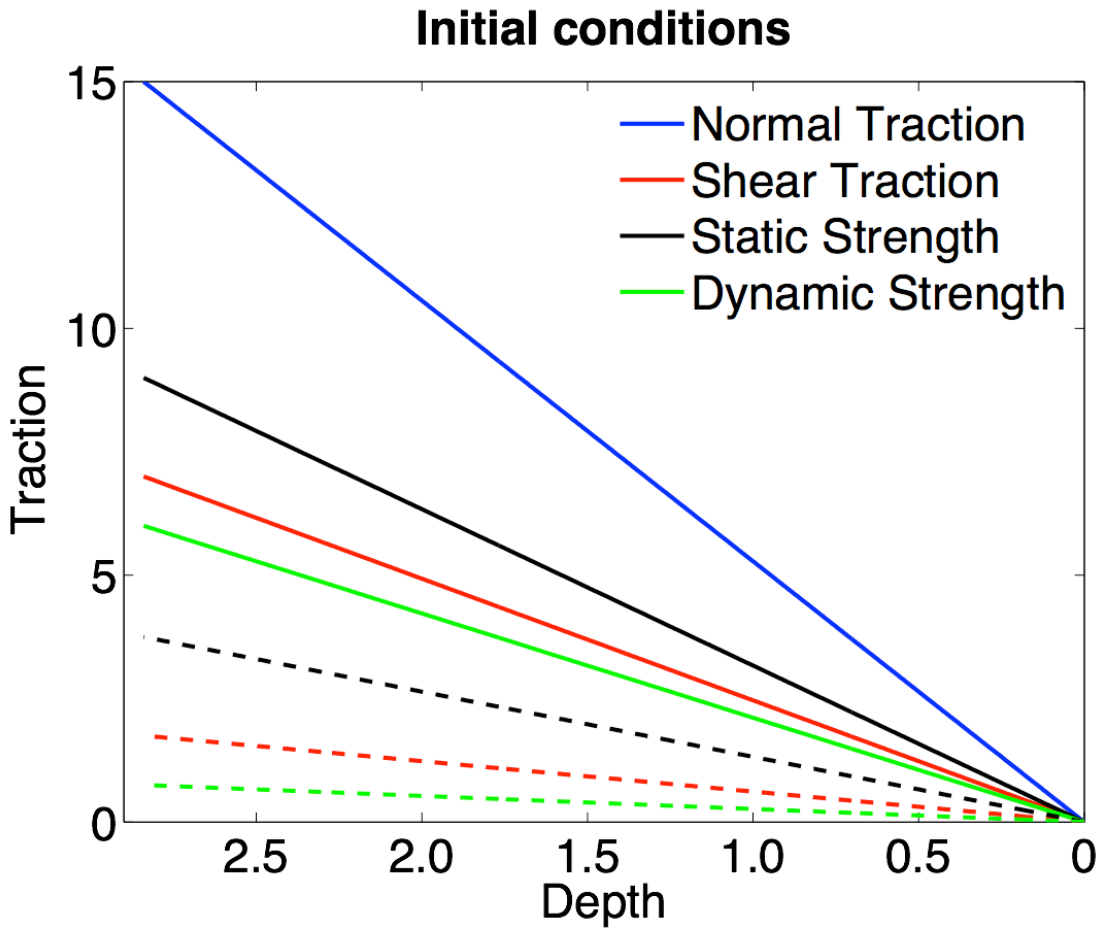


**Figure 2: Initial traction conditions as a function of depth. Both depth and traction are expressed in terms of dimensionless parameters. The blue line represents the normal traction profile that is the same for all the simulations. Red, black and green solid lines describe the initial shear traction, the static frictional strength and the dynamic frictional strength, respectively, for the simulations performed imposing the highest adopted friction level ($\mu_s = 0.60$; $\mu_d = 0.40$). Red, black and green dashed lines describe the initial shear traction, the static frictional strength and the dynamic strength level, respectively, for the simulations performed imposing the lowest used friction level ($\mu_s = 0.25$; $\mu_d = 0.05$).**

# 3. Results

## 3.1. Rupture dynamics and free surface waves interaction

We examine here the implication of the symmetry breaking due to the fault-wave interaction, on the rupture dynamics as the rupture propagates along the interface toward the free surface.

In Figure 3 we show the evolution of the slip rate (blue solid lines) and the normal traction perturbation (blue dashed lines). These curves are compared with the same quantities for the case where the interface is embedded in an unbounded medium under the same initial conditions (red curves). At the same time steps we also represent the kinetic energy density field in the medium for the simulations with free surface. In Figure 4, we show the absolute values of the first invariant (volumetric deformation) and of the second invariant (shear deviatoric deformation) of strain tensor at the same time steps as in Figure 3.

At the early stage of the rupture ($\tilde{t} = 2.3$) before the onset of the interaction, the slip rate profiles are overlapped (Figure 3a) and the waves emitted from the rupture have not yet reached the fault after being reflected/converted at the free surface. The normal traction perturbation at this stage is zero and the solutions are the same as the ones retrieved for the symmetric rupture propagating along a planar interface embedded in an infinite medium. The symmetry across the interface is also confirmed investigating the kinetic energy field (Figure 3b) and the deformation fields (Figure 4a-b) at the same time.

The Figure 3c shows the slip rate and the normal traction perturbation just after the onset of the interaction ($\tilde{t} = 4.6$). When the interaction starts, the rupture dynamics is affected at the crack front and behind the tip where the crack is sliding at the dynamic friction level. At this time, in the upward direction, the slip rate is enhanced at the crack front. Behind the process zone, the rupture undergoes an overshoot with a further increase of the slip rate. At this stage the maximum of the normal traction

perturbation is behind the process zone. This implies that the largest slip rate enhancement with respect to the unbounded case is observed in the region slipping at the dynamic friction level.

The blue dashed line in the Figure 3c evidences how the increase of slip rate is due to the symmetry breaking generated by the normal traction perturbation. Ahead of the crack front, wave interaction with the unslipping part of the interface produces a compression in the normal traction. Instead, at and behind the crack front the slip induced normal traction perturbation is tensile making the upward propagation favoured with respect to the symmetric case as supported from laboratory (Brune 1996) and numerical models (Nielsen 1998, Oglesby et al., 1998, 2000).

Wave interaction of the rupture with the free-surface is also shown through the kinetic energy density (Figure 3d) and the deformation fields (Figure4c, d). These quantities evidence the symmetry breaking in terms of non-uniform and increasing hanging-wall stored energy due to the reflected body and surface waves produced during the rupture propagation (Brune 1996; Shi et al. 1998). This in turn leads to a memory effect and to an increasing effective compliance of the hanging-wall. As such, the effect of breaking the reflection symmetry in this system resembles that of a bimaterial rupture advancing in the direction of the slip in more compliant medium (Andrews & Ben-Zion 1997; Harris & Day 1997; Rubin & Ampuero 2007; Scala et al., 2017).

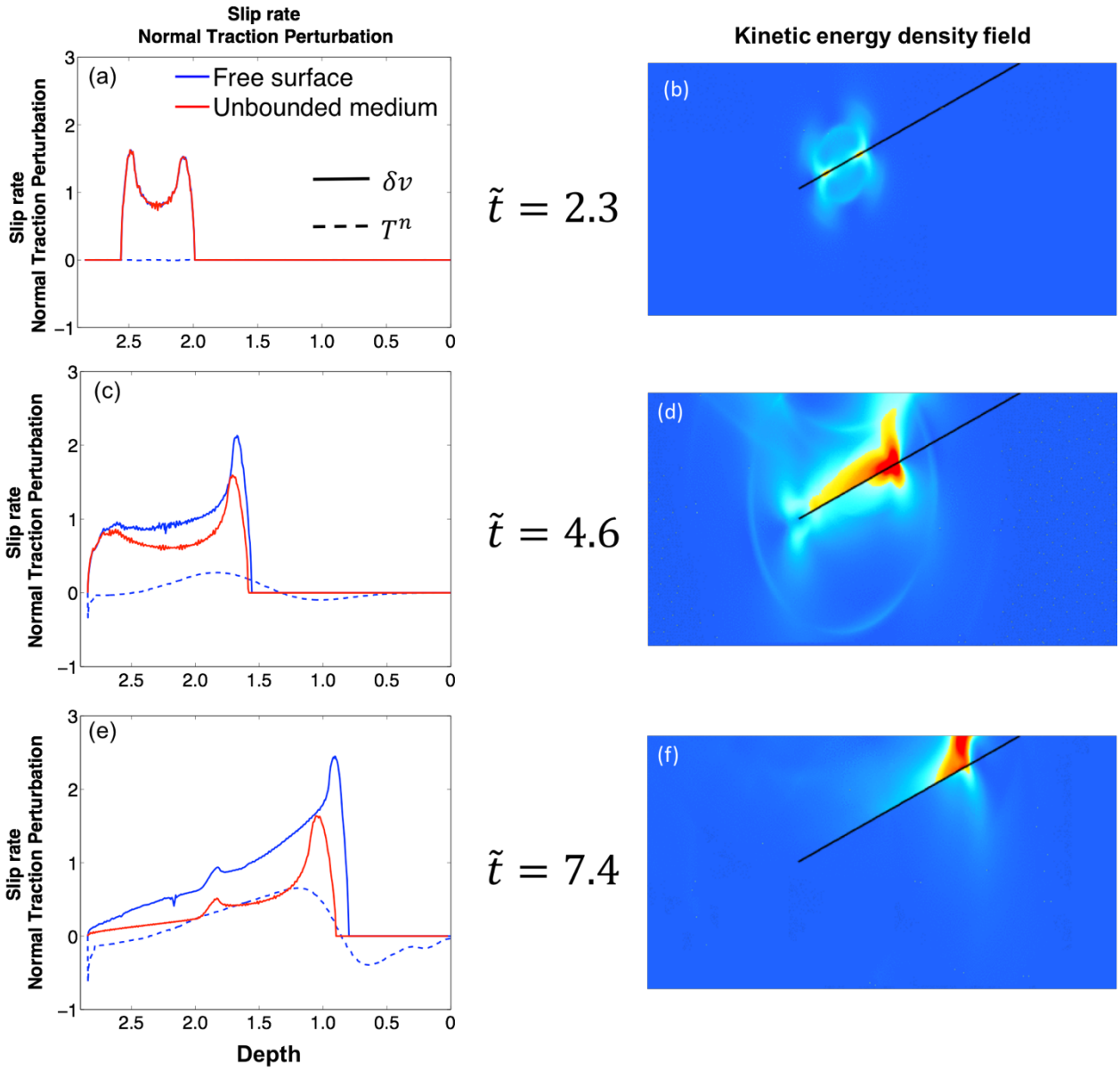


**Figure 3: On the left panels (a)-(c)-(e) the dimensionless slip rate (solid lines) and the normal traction perturbations (dashed lines) are plotted as a function of the normalized depth at the three time steps $\tilde{t} = 2.3; 4.6; 7.4$. The slip rate for the same simulation in an unbounded medium is plotted with a solid red curve (for the symmetric case the normal traction perturbation is zero). On the right-side, the panels (b)-(d)-(f) show, at the same time steps, the kinetic energy density field in the medium for the free surface simulation.**

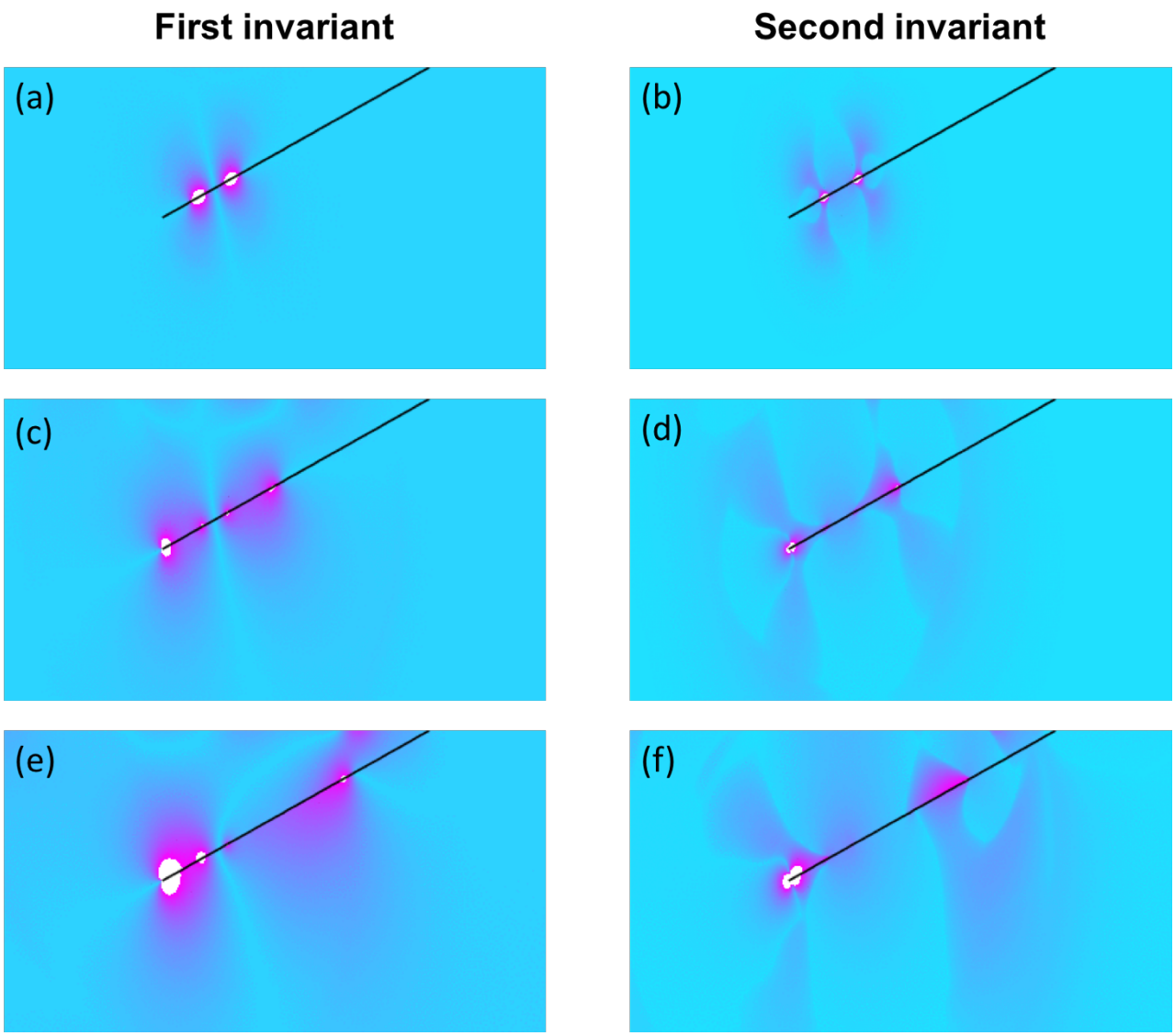


**Figure 4: For the same time steps of the Figure 3 the absolute value of the first (a-c-e) and of the second invariant (b-d-f) of the strain tensor is shown to the deform describe the volumetric and deviatoric deformation of the medium. An evident break symmetry breaking can be recognised in the snapshots (c-d-e-f) .**

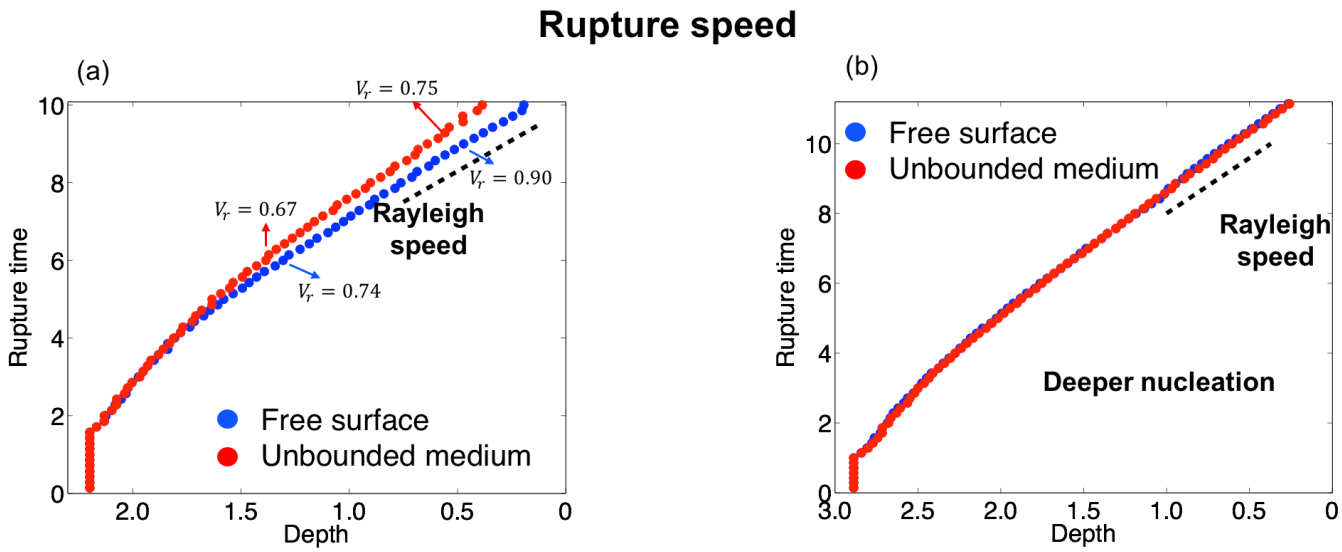


**Figure 5 Plots of rupture time as a function of depth. On the panel (a) the rupture time is shown for the free surface (blue dots) and unbounded medium (red dots) simulations of Figure 3. The black dashed line represents the slope corresponding to the Rayleigh speed in the medium. Both ruptures reach the asymptotic speed but at different time, as an effect of the inertia acquired by the rupture, when interacting with waves from the free surface. In the panel (b) the same quantities are plotted for a simulation having a deeper nucleation. When the asymptotic speed is reached before the wave-rupture interaction starts, the inertial effect can be neglected.**

As the rupture continues to propagate upward the symmetry breaking is strengthened. As a result, the slip rate and the normal traction perturbation increase more and more. At $\tilde{t} = 7.4$ the maximum of the slip rate at the crack front is more than twice larger than the corresponding value in an unbounded medium; the same effect is observed for the dynamic overshoot behind the process zone. In other words, when the rupture enters in the zone where the frictional strength and the stress drop are small enough to be comparable with the imposed level of cohesion, the rupture dynamics is dominated by the rupture- surface waves interaction and by the symmetry breaking. At this stage, most of the kinetic energy is concentrated in a narrow domain around the crack front (Figure 3f). In the vicinity of the surface, most of the energy from surface and body waves is stored in the hanging wall as emerging

from the deformation field in the medium (Figure 4e-f). This asymmetry is retrieved in the ground motion as supported by Nielsen (1998) and Oglesby et al. (2000).

To verify that the results are not affected by mesh-related artefact, a mesh refinement analysis has been performed. The same rupture dynamics has been simulated using a refined mesh with half of the mesh size. In Figure S2 of Supplementary information the slip rate curves at different stages of the dynamic rupture obtained with different mesh resolutions do superimpose, which warrant the numerical convergence of the simulations.

### 3.2. **Rupture speed and inertial** effect

The position of the crack tip in presence of a free surface (Figure 3e) in comparison with a crack propagating in an unbounded medium indicates that the free surface- rupture wave interaction has also an effect on the rupture acceleration and thus on the average rupture speed during the upward propagation.

Figure 4a shows the time of the slip activation along the interface, during the upward propagation as a function of the dimensionless depth $\tilde{z}$ both for the case with free surface (blue dots) and for the unbounded medium (red dots), for the same simulations of Figure 3. After the nucleation phase, the rupture speed is the same for the two cases, as long as the interaction is not triggered. When the interaction starts, the symmetry breaking causes a faster acceleration of the rupture. Finally, both ruptures accelerate toward the Rayleigh-wave speed expected as the asymptotic sub-shear limit for a rupture propagating in a homogenous medium (Burridge 1973).

In this simulation the interaction is triggered when the rupture speed is at ~60% of the S-wave velocity. Then the increasing symmetry breaking generates a sizeable acceleration effect. The rupture accelerates (Figure 5a) toward the asymptotic speed limit much faster in the asymmetric system than in the symmetric one.

The rupture speed, when reflection symmetry is broken, is ~10% larger at a normalized depth of ~1.2 and 20% larger in the vicinity of the surface as compared to the symmetric case. The values of the rupture velocity are reported in the Figure 5(a).

On the contrary, if the interaction starts when the rupture is close to the Rayleigh speed both the symmetric and the asymmetric ruptures proceed at the same numerical speed limit. This is illustrated in the Figure 5(b), for a numerical simulation realized with the same geometrical and initial conditions, but with a deeper nucleation.

When the rupture approaches the asymptotic speed limit the energy spent to further accelerate the rupture tends to zero, and the stored energy in the hanging-wall increases the effects of the symmetry breaking. This leads to a more pronounced increase of the maximum slip rate at the crack front and of the maximum of tensile normal traction perturbation as shown in the Figure S3 in the Supporting Information.

This non-classical rupture acceleration effect is a complex effect triggered by two coupled factors: first, the slip-induced tensile normal traction perturbation at and behind the crack tip leads to a weakening of the interface that promotes the upward rupture acceleration toward the asymptotic speed limit; second, effective inertial dynamics are inherited from wave interaction of the rupture with the free surface during the upward propagation giving rise to memory and effective hanging-wall mass.

The latter factor is supported by theoretical results (Marder 1991; Fineberg & Bouchbinder 2015) in the case of a crack propagating in an externally loaded infinite strip. Even if the system possesses a reflection symmetry, wave interaction of the rupture with boundaries leads to an energy release rate involving an inertial term and an effective mass, which decreases to zero as the rupture speed approaches the speed limit. Experimental results are also supporting these theoretical results evidencing a sluggish acceleration of the rupture in a strip, towards a speed limit lower than the Rayleigh-wave speed. Conversely, we have shown that the symmetry breaking in the case of dipping

357 reverse faults always favours the rupture acceleration towards the limit speed, owing to the slip-
358 induced tensile normal stress perturbation behind the crack tip.
359
360

361 ## 3.3. Friction level sensitivity

362 For symmetric ruptures in unbounded elastic media the energy balance is controlled by the frictional
363 strength and the stress drop all along the rupture propagation and therefore by the strength excess $s$.
364 The friction level does not modify the rupture dynamics as far as it does not affect these parameters.
365 Recent theoretical analysis has shown that, when the reflection symmetry across the interface is
366 broken by the effect of wave interaction of the rupture with boundary, the linear stability condition
367 governing the unstable dynamic propagation includes an explicit dependence on the friction level
368 (Aldam *et al.* 2016).
369 The slip rate and normal interface traction perturbation are shown Figure 6 for two numerical
370 experiments performed with different sets of friction coefficients ($\mu_s = 0.60 - \mu_d = 0.40$ and $\mu_s =$
371 $0.25 - \mu_d = 0.05$), at the same time steps than Figure 3.
372 At time $\tilde{t} = 2.3$ (Figure 6a) wave interaction of the rupture with the free surface has not yet been
373 triggered and the two solutions are identical and independent of the absolute level of friction.
374 After the triggering ($\tilde{t} = 4.6$, Figure 6b) the increase of the slip rate at and behind the crack front is
375 larger for the largest level of the friction. At this stage, both systems undergo a breaking of the
376 reflection symmetry, which is evidenced by a tensile slip-induced normal traction perturbation behind
377 the crack front, which is still undistinguishable between the two simulations.
378 At a later time ($\tilde{t} = 7.4$), the difference between the two systems in term of the maximum slip rate at
379 the crack front increases more and more. This is driven by difference in amplitude of the slip-induced
380 normal traction perturbation in the two cases (Figure 6c). When the reflection symmetry is broken,

the traction perturbation is triggered, and the coupling of the tangential slip with the normal traction increases with the level of friction.

The absolute level of friction is also affecting the rupture acceleration. The larger the friction level the faster is the acceleration towards the Rayleigh speed (Figure 7). This is to our knowledge a new result with important implications for reverse-fault rupture dynamics.

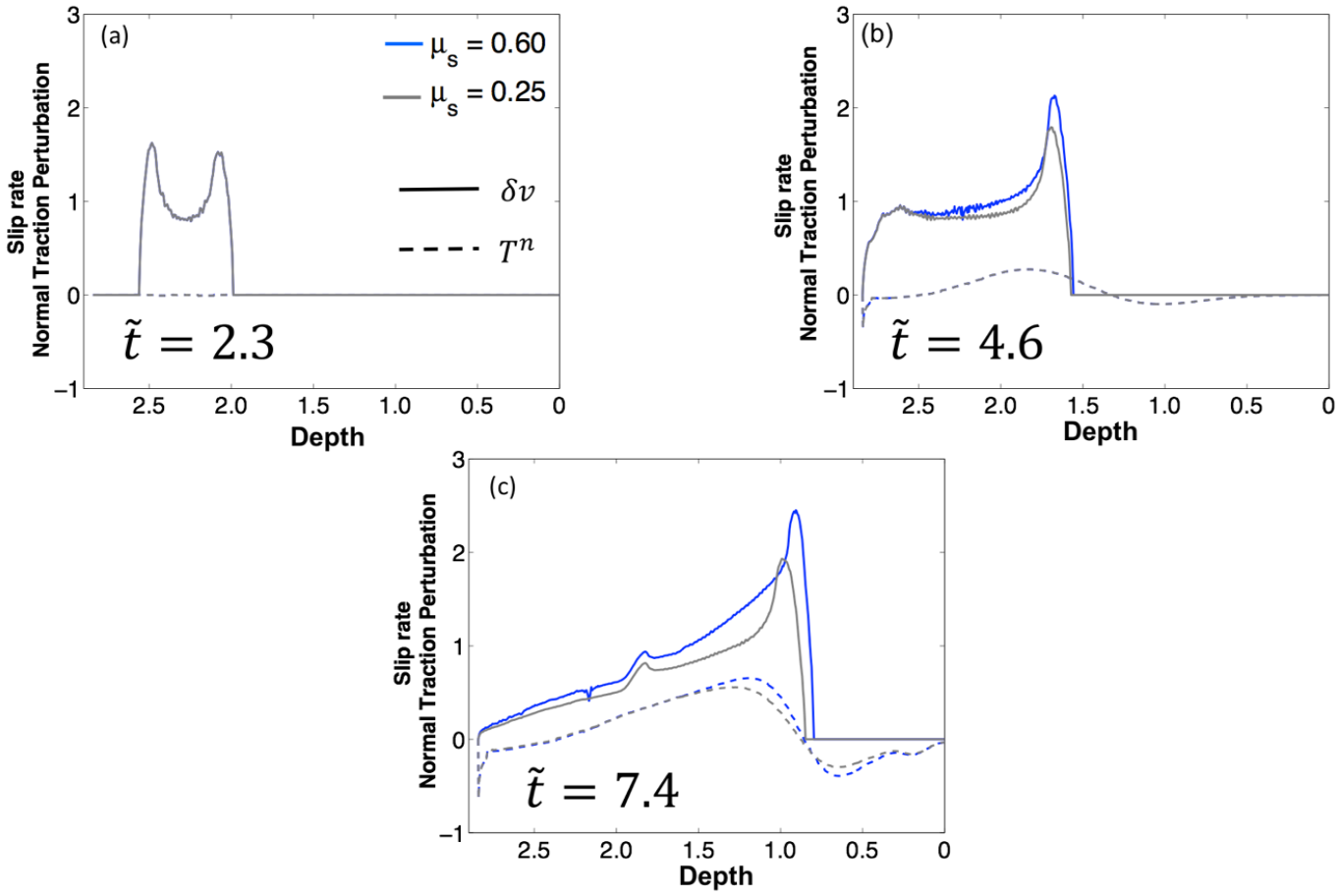


**Figure 6 Comparison between simulations with different friction levels. The slip rate (solid lines) and the normal traction perturbation (dashed lines) are plotted as a function of the normalized depth for two levels of friction at the same time steps of Figure 3. The blue curves are obtained for $\mu_s = 0.60$ and $\mu_d = 0.40$, the grey curves for $\mu_s = 0.25$ and $\mu_d = 0.05$**

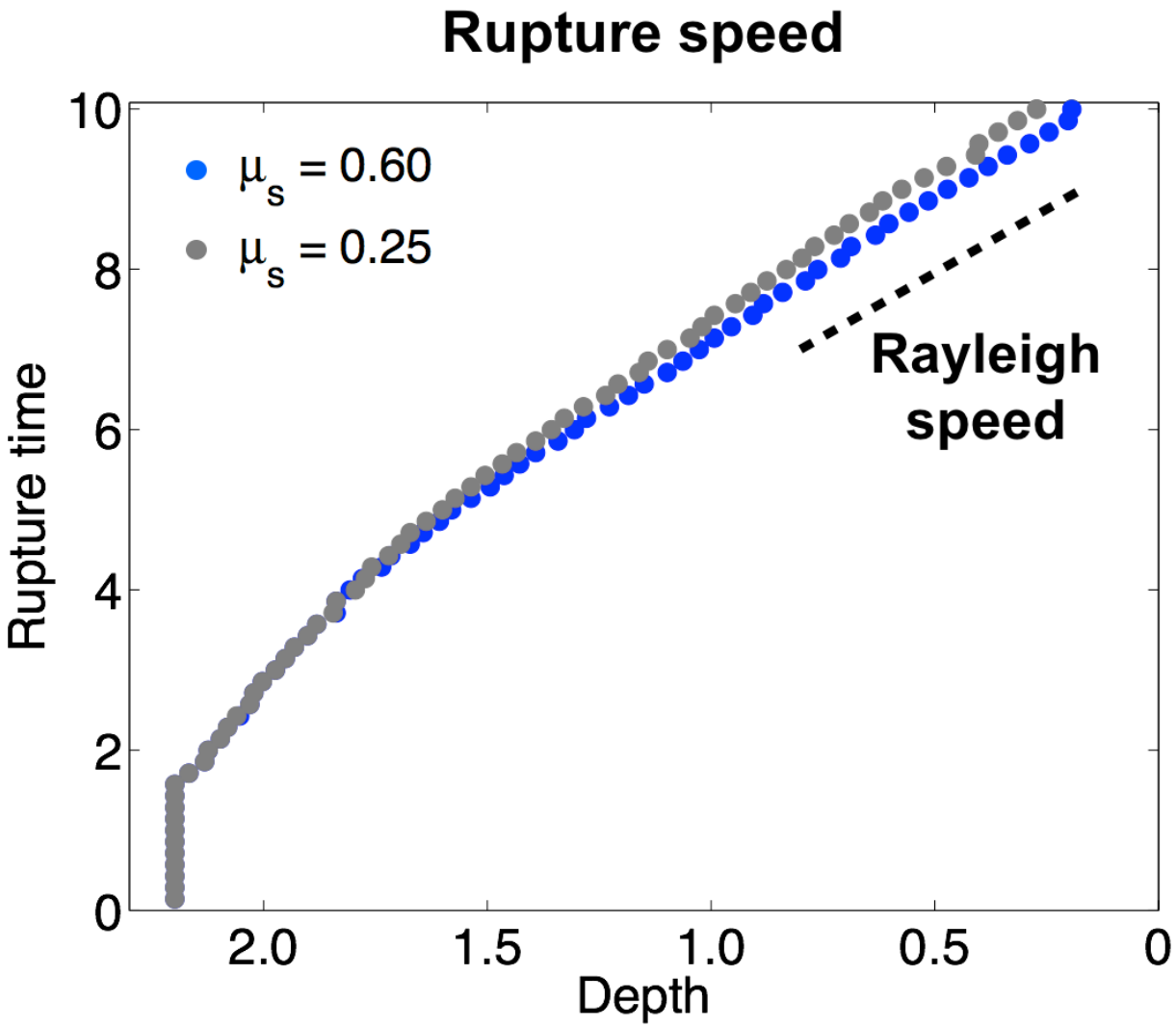


**Figure 7 Rupture time as a function of normalized depth for the two simulations with $\mu_s = 0.60$; $\mu_d = 0.40$, (blue dots) and $\mu_s = 0.25$; $\mu_d = 0.05$ (grey dots).**

### 3.4. Interface opening

In the previous subsection we have shown how reflection symmetry breaking, due to wave interaction of the rupture with the free surface, leads to a tensile slip-induced normal traction perturbation at and behind the crack front.

As the rupture propagates up-dip, the tensile slip-induced traction perturbation occurs in regions of the fault where the initial normal traction is smaller and smaller. Thus, in the vicinity of the free

surface, the initial normal traction becomes small enough to possibly allow an opening of the interface.

Figure 8 shows, at the dimensionless time-step $\tilde{t} = 10.7$, the distributions of the slip rate and normal traction perturbation for the two simulations described in the previous sub-section.

For the largest friction level (blue curves), an opening of the interface starts at the crack tip and then, almost instantaneously, propagates towards the surface, through the portion of the interface where a compressive perturbation was previously induced by the waves. This portion has a finite length and after the opening it no longer comes back in contact, behaving as a free surface. The separation between the frictionally sliding portion of the interface (where a slip rate is defined and the total normal traction is negative) and the opened part of the interface (where total normal traction is zero) is marked in the Figure 7 by a black dashed line. At this point the asymmetric deformation around the propagating crack front is instantaneously released as an effect of the end of the frictional propagation (Figure S4 in the Supporting information).

For system that possesses reflection symmetry (unbounded system) we never observe an opening of the interface, even if the topmost point of the interface has zero normal traction to mimic the same initial conditions.

The intensity of the slip-induced normal traction perturbation effect depends on the friction. In Figure 8, at $\tilde{t} = 10.7$, the solid and dashed grey curves represent the slip rate and the normal traction perturbation for the two sets of friction. For lower friction no opening occurs, and frictional slip may propagate up to the free surface.

For the same initial traction conditions, the opening effect is both controlled by the nucleation depth and the friction level. Figure 9(a) shows the opening length as a function of the barycentre of the nucleation patch. The deeper the nucleation the larger the opening length is. Since a larger opening domain implies a stronger induced normal traction perturbation, this effect is due to the larger amount of radiation emitted by the rupture and stored in the hanging wall. Similar results are obtained as a

function of the static level of friction: the larger the friction values the longer the opening patch is (Figure 9b).

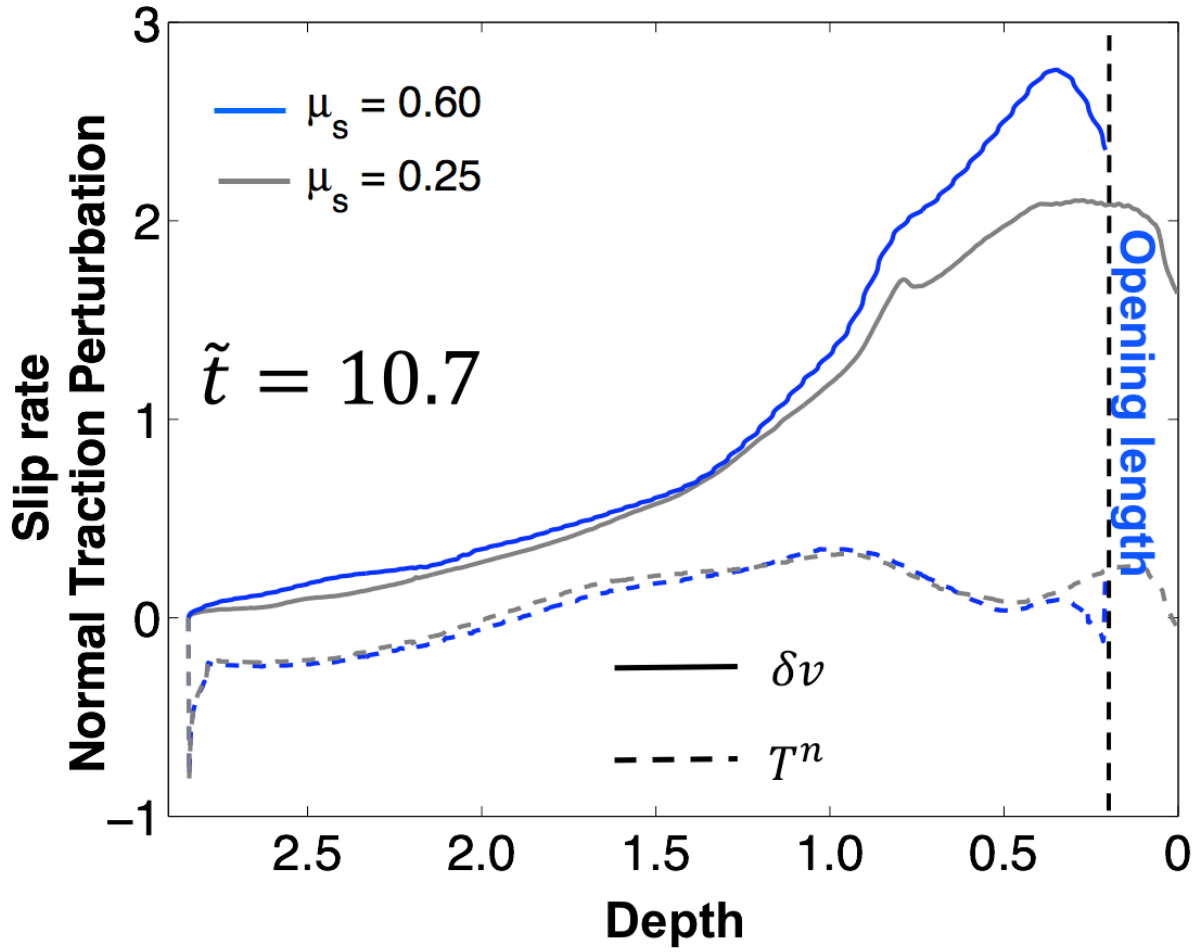


**Figure 8. Slip rate (solid lines) and normal traction perturbation (dashed lines) plotted as a function of depth for $\mu_s = 0.60$; $\mu_d = 0.40$ (blue dots) and for $\mu_s = 0.25$; $\mu_d = 0.05$ (grey dots). The black vertical dashed line marks the opening domain for the simulation with $\mu_s = 0.60$.**

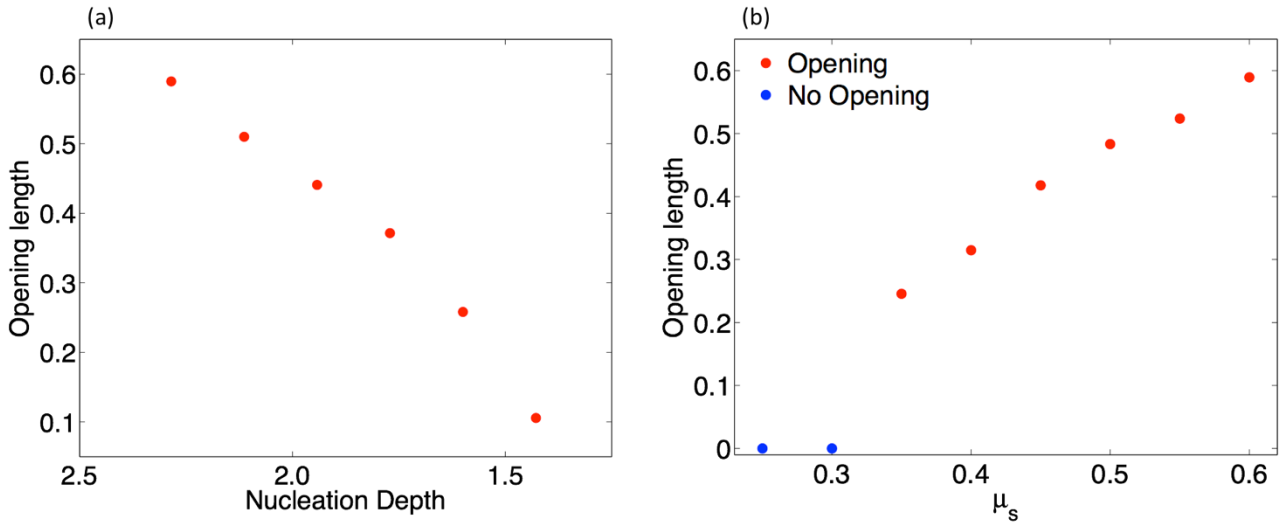


**Figure 9: In the panel (a) the opening length is plotted as a function of the nucleation depth. In the panel (b) the opening length is plotted as a function of static friction coefficient. The blue dots indicate that for small friction values the opening does not occur. The opening length increases with both nucleation depth and friction level.**

## 3.5. Shallow slip and surface displacement

In all simulations, strong and asymmetric ground motion and surface deformation are the signature of an asymmetric distribution of the kinetic and of the history-dependent stored energy that results from the geometric broken reflection symmetry across the interface as the the rupture propagates upward. This is supported by previous numerical results (e.g. Nielsen, 1998; Oglesby et al, 2000). Figure 10a shows the co-seismic slip distribution, as a function of the depth, along the interface for two different cases with the same dipping-interface geometry and nucleation depth, but with different absolute level of friction, e.g. ($\mu_s = 0.6$ - $\mu_d = 0.4$) and ($\mu_s = 0.25$ - $\mu_d = 0.05$). For comparison, result for the latter friction condition but in a system that possesses reflection symmetry (unbounded medium) is also added.

While for asymmetric system the maximum interface slip is concentrated around the nucleation zone; the symmetry breaking leads to large amplitude slip that increases along the upward portion of the interface and reaches a kind of plateau, for both sets of friction. The higher the friction, the larger is

the maximum slip amplitude. Slip in the vicinity of the free surface is generally about three to four times large that in the unbounded case.

Figure 10b shows the static vertical displacement along the free surface, as a function of the horizon distance measured from the intersection of the frictional interface with the free surface. Strong uplift on the hanging-wall side, close to the interface, is the signature of geometric reflection asymmetry as a result of the wave interaction history of the rupture with the free surface. As such the static vertical displacement depends also on the absolute level of friction of the interface.

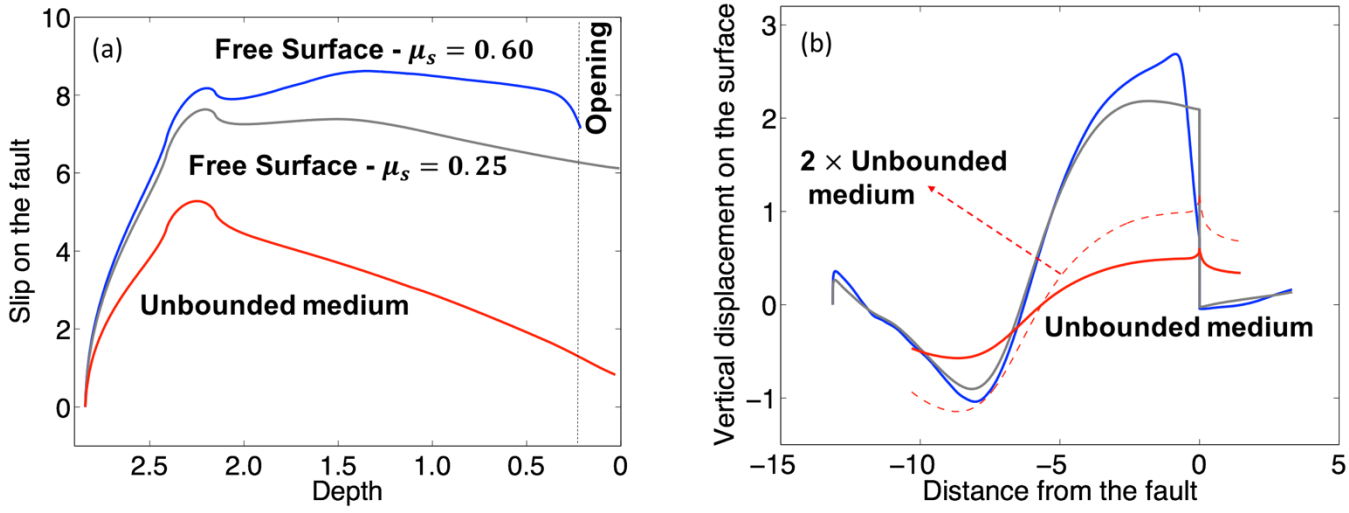


**Figure 10: In the panel (a) the final slip on the fault is plotted as a function of depth for an unbounded simulation (red curve), a free surface simulation with the lowest level of friction (grey curve) and a free surface simulation with the highest level of friction (blue curve). The vertical dashed line marks the opening domain for this latter simulation. In the panel (b), for the same simulations, the static vertical displacement is plotted as a function of the horizontal distance from the point of the fault on the surface. Negative values represent points on the hanging-wall (See Figure 1) while positive ones refer to points on the footwall. The red dashed line is the result of the solid line multiplied by two, this factor accounting at the first order for the free surface effect.**

## 3.6. Interface cohesion

In this model, small stress perturbations driven by waves may induce episodic unrealistic sliding near the free surface disconnected from the mother crack, since the frictional strength goes to zero in the

476 upper portion of the interface. The use of a small, though non-zero cohesion helps in limiting this
477 effect.
478 To evaluate the influence of the interface cohesion, we compare the solutions obtained in the previous
479 sections with simulations where $C = 0$. In Figure 11 we compare the slip rate and the normal traction
480 perturbation for the same system as in Figure 3 at two different time steps during the rupture
481 propagation. The different energy balance, due to the lack of the cohesion, leads to an enhanced up-
482 dip propagation in terms of both maximum of slip rate at the crack front and rupture velocity (black
483 curves).
484 When there is no interface cohesion, a secondary crack emerges ahead of the rupture front, increasing
485 the compressive perturbation ahead the mother rupture front associated with seismic waves. The
486 secondary crack propagates up to the free surface. while it is initially suppressed by the use of a
487 cohesion (Figure 11a) and emerges later close to the surface (Figure 11b).
488 It is worth to note that, despite different energy balance slightly changes the rupture dynamics
489 between the two cases, the cohesion does not change the qualitative behaviour of the rupture
490 dynamics, the rupture-wave interaction, the changes in the rupture speed and the interface opening
491 features.
492 In the case where $C \neq 0$, when the normal traction goes to zero (opening condition), an instantaneous
493 stress drop by an amount of $C$ occurs, transferring elastodynamic energy around the opened portion
494 of the interface. However, due to the low cohesion level, this energy is negligible compared to the
495 energy stored in the hanging-wall and no significant dynamic effect emerges. Moreover, this stress
496 drop does not trigger spurious effect on the results as shown by the grid refinement analysis.
497

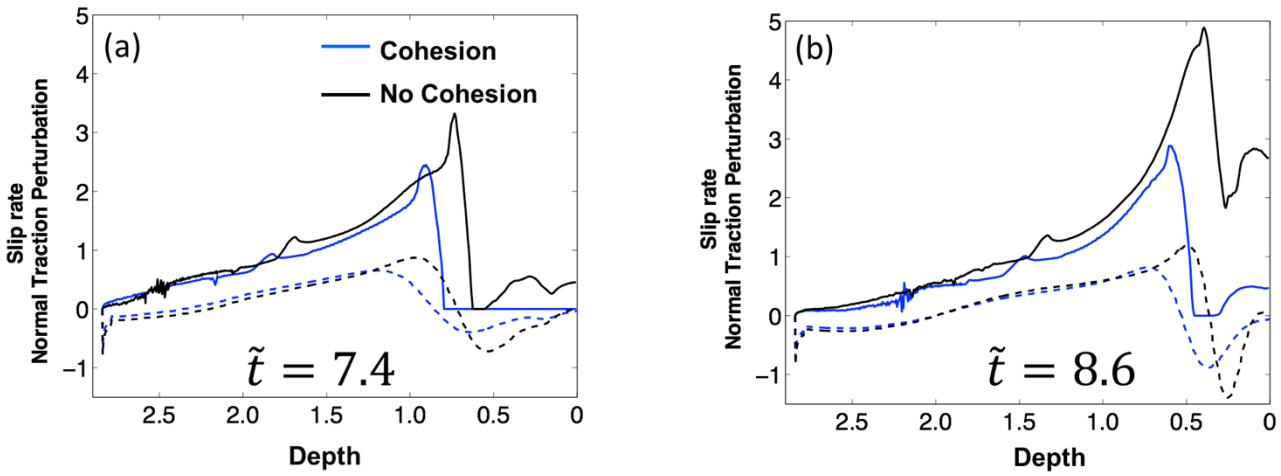


**Figure 11 Comparison between two simulations for which the $C \neq 0$ (blue curves) and $C = 0$ (black curves). Panels (a) and (b) refer to the dimension less time $\tilde{t} = 7.4$ and $\tilde{t} = 8.6$ respectively. Solid and dashed lines show the spatial distribution of the slip rate and the normal traction perturbation respectively.**

## 4. Discussion and conclusions

In this work, combining different numerical experiments, we deeply investigated how the dynamics of a thrust rupture reaching the surface is controlled by the symmetry breaking due to the interaction of the fault interface with the seismic waves in the vicinity of the free surface.

Seismic waves radiated during the rupture propagation get reflected/converted at the free surface and trigger a rupture/surface interaction when they reach the crack again. As such the crack is interacting with its own history giving rise to memory. Using simple geometrical considerations, the distance $d_i$ from the free surface at which this interaction affects the crack tip depends on the nucleation depth $d_n$, the dip angle $\theta$, the S-wave velocity $V_s$, and the average rupture speed $\hat{V}_r$, according to the formula:

$$d_i = d_n \left( 1 - \frac{\hat{V}_r \cdot \sin\theta}{\sqrt{V_s^2 - \hat{V}_r^2 \cdot \cos^2\theta}} \right) \tag{4}$$

This quantity is normalized by a characteristic length scale of the problem that is expressed in the eq. (4) by the nucleation depth; the faster the rupture the shallower the trigger of the interaction. More

516 details about this geometrical interpretation are provided in the Supporting Information (See Figure
517 S5 and the related text).
518 We finely investigated how this wave interaction controls the coupling between the shear and the
519 normal traction perturbation, which is shown to be compressive ahead of the crack front and
520 extensional behind it. Signature of this geometric breaking of the reflection symmetry can be found
521 on the radiated energy and the history-dependent stored energy in the hanging-wall. As a result, the
522 surface ground motion is also asymmetric as also evidenced by previous numerical and laboratory
523 studies (Nielsen 1998; Oglesby et al. 1998, 2000; Uenishi 2015; Ma & Archuleta 2016) and expected
524 from seismological observations (Abrahamson & Sommerville 1996; Vallage et al. 2015). We found
525 that the symmetry breaking leads to an enhancement of the slip rate at the crack-tip, associated with
526 a sudden decrease of frictional strength similarly to a bimaterial interface case (Harris & Day 1997).
527 We also found as a new result that the geometric asymmetry induced by the wave interaction of the
528 rupture with the free surface drives faster acceleration of the rupture towards the asymptotic Rayleigh-
529 wave speed limit than in a symmetric configuration. This is due to the tensile normal traction
530 perturbation and inherited inertial dynamics involving a velocity-dependent effective mass (Marder
531 1991). This is in contrast with the rupture propagation within an infinite strip, where the inertia
532 dynamics inherited from rupture/wave interaction reduce the acceleration of the rupture towards the
533 limit speed (Goldman 2010, Fineberg & Bouchbinder 2015). It is worth to note here that in our
534 idealised reverse-fault, the stronger acceleration does not lead to a short rupture time. Indeed, the
535 rupture does not arrest when it impacts against the free-surface because the surface waves trapped in
536 the hanging-wall continue to sustain the slip growth with time leading to average longer rupture
537 durations for ruptures lacking the reflection symmetry.
538 An important outcome of this study is that the symmetry breaking leads to a dependence of the rupture
539 dynamics on the absolute level of friction: a higher level of friction induces larger amplitude of the
540 slip-induced normal traction perturbations which in turn favour the up-dip rupture propagation
541 increasing the inertia effect and the slip rate enhancement. This result are supported by linear stability

542 analysis (Aldam, et al, 2016) showing a frictional dependence of the sliding for a system that lacks
543 reflection symmetry across the interface.
544 We then found that when the rupture propagates along the shallowest portion of the interface, where
545 the initial normal traction and stress drop decrease, the tensile traction perturbation may lead to an
546 interface opening. This feature propagates almost instantaneously up to the free surface with the two
547 sides of the interface separating along a finite length of the interface. We also found that the opening
548 effect is also dependent on the frictional level and the rupture propagation distance from the
549 nucleation, and for small values of the friction the opening does not occur.
550 Recent laboratory study (Gabuchian et al. 2017) also supported the possibility of an interface opening
551 as a result of a torque mechanism. Such torque mechanism might result from large deformations as
552 the rupture approaches the free surface, which are not investigated in this study, where the simulations
553 are performed under a small deformation hypothesis.
554 Beyond this, the opening effect of a crack reaching the free surface has been already shown in the
555 numerical experiments by Shi et al. (1998), confirming the laboratory results by Brune (1996).
556 However, diversely from these models the features of the opening are different. In our model, where
557 the tectonic loading increases with depth, with small normal and tangential traction close to the
558 surface, the opening is limited to a region close to the surface and does not propagate back along the
559 fault. In addition, the two sides of the fault do no longer come in contact after the opening. The use
560 of a high-resolution numerical method with non smooth contact and friction conditions, such as the
561 spectral element method, allows to characterize how the opening is generated, and to analyse the size
562 of the opening region as a function of the friction coefficient and the nucleation depth.
563 As a direct implication of this study, we showed that in our model the effect of wave interaction of
564 the rupture with the free surface drives strong amplification and asymmetry of shallow slip and large
565 vertical static surface displacement, which have important implication in terms of tsunami source and
566 tsunami potential for an off-shore event. Recent studies have shown that a large amount of slip from
567 several thrust earthquakes concentrates along the shallower part of the fault both at large collision

568 zones (e.g., in the case of the 1999, $M_w$7.7 Chi-Chi earthquake, Tanaka et al. 2006, Zhang et al. 2008)
569 and along subduction interfaces, such as for the $M_w$ 9.2 2004 Sumatra earthquake and the 2011,
570 $M_w$ 9.1 Tohoku earthquake (Shearer & Burgmann 2010, Romano et al., 2014, Lorito et al. 2016, Lay
571 2018). The unexpectedly large slip in the shallow low-rigidity portion of the subducting plate was
572 identified as responsible for the huge tsunami waves that devastated the near coastal areas (e.g., Mori
573 et al. 2011, Satake et al. 2013). Moreover, the longer average rupture duration is a feature commonly
574 observed for shallow earthquakes (Bilek & Lay,1999; Geist & Bilek, 2001) as well as for the so-
575 called tsunami earthquakes such as the historical 1896, $M_s$ 7.2 Sanriku (Tanioka & Satake, 1996b)
576 and the 2010, $M_w$ 7.8 Mentawai earthquakes (Yue et al. 2015). In our results, all these effects are
577 shown to be dependent on the level of friction and they are always significant when compared to the
578 symmetric case.
579 Broken reflection symmetry in reverse-fault systems can also be constitutive in nature, and more
580 realistic reverse-fault models could include softer shallow layers, such as accretionary prisms in
581 subduction zones, and inelastic dissipative mechanisms in the hanging-wall (e.g., Ma & Beroza, 2008;
582 Ma, 2012; Ma & Hirakawa, 2013, Kozdom & Dunham, 2013; Lotto et al, 2017). When rupture enters
583 or interacts with such layers the absolute value of the rupture speed might decrease even for a constant
584 ratio between the rupture speed and the S-wave speed (Murphy et al, 2018). Constitutive bi-material
585 might enhance the effect of the wave interaction of the rupture with the free surface, and increase the
586 coupling between interfacial slip and normal traction perturbation (e.g. Ma & Beroza, 2008). This
587 can contribute to increase the rupture duration in the case of shallow events. Moreover, small friction
588 levels in the vicinity of shallow accretionary sediments might affect the amplification of the vertical
589 ground motion (Murphy, 2018). Inelastic dissipation effects in the hanging-wall, such as off-fault
590 damage or plasticity (Thomas & Bhat, 2018), may also contribute in the ground motion damping.
591 We selected a single dip angle for our simulation (20°) that corresponds to an intermediate value for
592 some subducting interfaces, between the very low dip angles in the vicinity of the oceanic trenches
593 (Kozdon & Dunham 2013) and the steepest slopes revealed by seismic imaging at larger depths

(Takahashi et al. 2004; Satriano et al. 2014). A more extended parametric study might allow to asses more quantitatively the wave interaction effect of the rupture with the free surface, as a function for example of the dip angle and of the initial traction profile along the interface. Nevertheless, as long as the hypothesis of increasing initial normal traction with depth can be considered valid, the interpretation framework provided in this study can be at least qualitatively extended to interfaces with smaller dip angles.

Finally, since no system is perfectly symmetric, we believe that geometrically-induced coupling between interfacial slip and normal traction perturbation, induced by wave interaction of the rupture with boundaries, may exist in a broad range of frictional fault systems. Consequently, coupling of seismic waves with the rupture should be incorporated in various numerical approaches and when interpreting geophysical observations.

## Acknowledgements

The data for this paper can be accessed at the doi: https://doi.org/10.6084/m9.figshare.6940805.

The authors would like to thank Harsha Bhat and Raul Madariaga for fruitful scientific discussion during this work. The numerical simulations were performed with the support of the High-Performance Computing Auriga cluster at INGV, with the support of Daniele Melini, and on the High-Performance Computing and Data Analysis platform (S-CAPAD) at IPGP, with the support of Geneviève Moguilny.

620

# 621 Bibliography

622

623 Abrahamson, N. A. & Sommerville, P.G. (1996). Effects of the Hanging-wall and Footwall on
624 Ground Motions Recorded During the Northridge Earthquake. *Bulletin of Seismological Soxiety of*
625 *America* 86(1B): S93-S99.

626

627 Aldam M., Bar-Sinai Y., Svetlizky I., Brener E. A., Fineberg J., & Bouchbinder E., (2016). Frictional
628 Sliding without Geometrical Reflection Symmetry. *Physical Review* Vol. 6, 041023. doi:
629 10.1103/PhysRevX.6.041023.

630

631 Andrews, D.J. & Ben-Zion, Y., (1997). Wrinkle-like slip pulse on a fault between different materials,
632 *Journal of Geophysical Research*, 102, 553–571. doi: 10.1029/96JB02856.

633

634 Bilek S. L., & Lay T., (1999). Rigidity Variations With Depth Along Interplate Megathrust Faults in
635 Subduction Zones. *Nature,* Vol. 400: 443-446. doi: 10.1038/22739.

636

637 Brener E. A., Weikamp M., Spatschek R., Bar-Sinai Y. & Bouchbinder E. (2016). Dynamic
638 Instabilities of Frictional Sliding at a Bimaterial Interface. *Journal of the Mechanics and Physics of*
639 *Solids,* Vol. 89: pp. 149-173. doi: 10.1016/j.jmps.2016.01.009.

640

641 Burridge, R., (1973). Admissible Speeds for Plane-Strain Self-Similar Shear Cracks With Friction
642 but Lacking Cohesion, *Geophysical Journal International* Vol. 35(4): 439–455. doi: 10.1111/j.1365-
643 246X.1973.tb00608.x.

644

645 Erdogan F. & Arin K., (1975), Half plane and a slip with an arbitrary located crack, *International*
646 *Journal of Fracture*, Vol. 11
647
648 Festa, G., Delavaud E. & Vilotte J.-P. (2005). Interaction Between Surface Waves and Absorbing
649 Boundaries for Wave Propagation in Geological Basins: 2D Numerical Simulations, *Geophysical*
650 *Research Letters*, Vol. 32(20), L20306. doi:10.1029/2005GL024091.
651
652 Festa, G. & Vilotte J.-P. (2005). The Newmark Scheme as Velocity-Stress Time-Staggering: an
653 Efficient Implementation for Spectral Element Simulations of Elastodynamics, *Geophysical Journal*
654 *International*, Vol.161(3), pp789-812. doi: 10.1111/j.1365-246X.2005.02601.x.
655
656 Festa, G. & Vilotte J.-P. (2006). Influence of Rupture Initiation on the Intersonic Transition: Crack-
657 Like versus Pulse-Like Modes, *Geophysical. Research Letters*, Vol. 33(15), L15320. doi:
658 10.1029/2006GL026378.
659
660 Fineberg, J & Bouchbinder, E. (2015). Recent developments in dynamic fracture: Some perspectives.
661 *International Journal of Fracture,* 196, pp. 33-57. arXiv 1504.04851
662
663 Gabuchian V., Rosakis A. J., Lapusta N., & Oglesby D. D., (2014). Experimental Investigation of
664 Strong Ground Motion Due to Thrust Fault Earthquakes. *Journal of Geophysical Research: Solid*
665 *Earth,* Vol. 119(2), pp. 1316-1336. doi: 10.1002/2013JB010409.
666
667 Gabuchian V., Rosakis A. J., Bhat H. S., Madariaga R., & Kanamori H., (2017). Experimental
668 Evidence that Thrust Earthquake Ruptures Might Open Faults. *Nature* Vol. 545(7654): pp. 336-339.
669 doi: 10.1038/nature22045.
670

671 Geist, E.L., & Bilek, S.L. (2001). Effect of Depth-Dependent Shear Modulus on Tsunami Generation
672 Along Subduction Zones. *Geophysical Research Letters* Vol. 28(7): pp. 1315-1318 doi:
673 10.1029/2000GL012385.
674
675 Goldman T., Livne A., & Fineberg J., (2010). Acquisition of Inertia by a Moving Crack. *Physical*
676 *Review Letters.* Vol. 104: 114301. doi: 10.1103/PhysRevLett.104.114301.
677
678 Harris, R.A. & Day, S.M., (1997). Effects of a low-velocity zone on a dynamic rupture, *Bulletin of*
679 *Seismological Society of America*, 87, 1267–1280.
680
681 Huang Y., Meng L., & Ampuero J.-P. (2012). A Dynamic Model of the Frequency-Dependent
682 Rupture Process of the 2011 Tohoku-Oki Earthquake. *Earth Planets Space,* Vol. 64, pp. 1061-1066.
683 doi: 10.5047/eps.2012.05.011.
684
685 Ida, Y. (1972). Cohesive force across the tip of a longitudinal-shear crack and Griffith's specific
686 surface energy, *Journal of Geophysical Research*, Vol. 77: 3796–3805. doi:
687 10.1029/JB077i020p03796.
688
689 Komatitsch, D. & Vilotte, J.-P., (1998). The Spectral Element Method: an Efficient Tool to Simulate
690 the Seismic Response of 2D and 3D Geological Structures, *Bulletin of Seismological Society of*
691 *America*, Vol 88: 368–392.
692
693 Kozdon, J. E. & Dunham E. M. (2013), Rupture to the Trench: Dynamic Rupture Simulations of the
694 11 March 2011 Tohoku Earthquake, *Bulletin of the Seismological Society of America*, Vol. 103(2B):
695 pp 1275-1289. doi:10.1785/0120120136.
696

Lay, T., (2018). A Review of the Rupture Characteristics of the 2011 Tohoku-oki Mw 9.1 Earthquake. *Tectonophysics* Vol. 733. doi: 10.1016/j.tecto.2017.09.022.

Lorito S., Romano, F. & Lay, T., (2016). Tsunamigenic Major and Great Earthquakes (2004–2013): Source Processes Inverted from Seismic, Geodetic, and Sea-Level Data. In: *Springer Encyclopedia of Complexity and System Science*. Springer Science + Business Media, New York, pp. 1–52. doi: 10.1007/978-3-642- 27737-5_641-1.

Ma, S. (2012). A self-consistent mechanism for slow dynamic deformation and tsunami generation for earthquakes in the shallow subduction zone, *Geophysical Research Letters*, 39, L11310, doi:10.1029/2012GL051854.

Ma, S., & Archuleta R. J. (2006). Radiated seismic energy based on dynamic rupture models of faulting, *Journal of Geophysical Research,* 111, B05315, doi: 10.1029/2005JB004055.

Ma, S., & Hirakawa E. T. (2013). Dynamic wedge failure reveals anomalous energy radiation of shallow subduction earthquakes, *Earth and Planetary Science Letters,* 375, pp. 113-122, doi: 10.1016/j.epsl.2013.05.016

Marder M. (1991). New Dynamical Equation for Cracks. *Physical Review Letters.* Vol. 66(13): pp. 2484-2488. doi: 10.1103/PhysRevLett.66.2484.

Murphy S., Scala A., Herrero A., Lorito S., Festa G., Trasatti E., Tonini R., Romano R., Molinari I. & Nielsen S., (2016). Shallow Slip Amplification and Enhanced Tsunami Hazard Unravelled by Dynamic Simulations of Mega-Thrust Earthquakes. *Scientific Reports* Vol. 6, 35007. doi: 10.1038/srep35007.

723

724 Murphy S., Di Toro G., Romano R., Scala A, Lorito S., Spagnuolo E., Aretusini S., Festa G., Piatanesi
725 A. & Nielsen S., (2018). Tsunamigenic Earthquake Simulations Using Experimentally Derived
726 Friction Laws. *Earth and Planetary Science Letters,* Vol. 486, pp. 155-165. doi:
727 10.1016/j.epsl.2018.01.011.

728

729 Mori, N., Takahashi, T., Yasuda, T. & Yanagisawa, H. (2011). Survey of 2011 Tohoku Earthquake
730 Tsunami Inundation and Run-up. *Geophysical Research Letters,* Vol. 38, L00G14, doi:
731 10.1029/2011GL049210.

732

733 Nielsen, S. B., (1998). Free Surface Effects on the Propagation of Dynamic Rupture, *Geophysical*
734 *Research Letters,* Vol. 25(1): 125-128. doi: 10.1029/97GL03445.

735

736 Oglesby, D. D., Archuleta R., J., & Nielsen S., B., (1998). Earthquakes on Dipping Faults: the Effects
737 of Broken Symmetry, *Science,* Vol. 280(5366): 1055-1059. doi: 10.1126/science.280.5366.1055

738

739 Oglesby, D. D., Archuleta R., J., & Nielsen S., B., (2000). Dynamics of Dip-Slip Faulting:
740 Explorations in two dimensions, *Journal of Geophysical Research,* Vol 105(B6): 13,643-13,653. doi:
741 10.1029/2000JB900055.

742

743 Romano F., Trasatti E., Lorito S., Piromallo C., Piatanesi A., Ito Y., Zhao D., Hirata K., Lanucara P.
744 & Cocco M., (2014). Structural Control on the Tohoku Earthquake Rupture Process Investigated by
745 3D FEM, Tsunami and Geodetic Data. *Scientific Reports* Vol 4: 5631. doi: 10.1038/srep05631.

746

747 Rubin A.M., & Ampuero J.-P. (2007). Aftershock Asymmetry on a Bimaterial Interface. *Journal of*
748 *Geophysical Research: Solid Earth* 112: B05307. doi: 10.1029/2006JB004337.

749

750 Rudnicki, J. W. & Wu, M. (1995). Mechanics of Dip-Slip Faulting in an Elastic Half-Space. *Journal*
751 *of Geophysical Research,* Vol. 100: 22173–22186. doi: 10.1029/95JB02246.

752

753 Satake, K., Fujii, Y., Harada, T. & Namegaya, Y. (2013). Time and Space Distribution of Coseismic
754 Slip of the 2011 Tohoku Earthquake as Inferred from Tsunami Waveform Data. *Bulletin of the*
755 *Seismological Society of America,* Vol. 103(2B): 1473–1492. doi: 10.1785/0120120122.

756

757 Satriano C., Dionicio V., Miyake H., Uchida N., Vilotte J.-P., & Bernard P., (2014). Structural and
758 Thermal Control of Seismic Activity and Megathrust Rupture Dynamics in Subduction Zones:
759 Lessons from the Mw 9.0, 2011 Tohoku earthquake. *Earth and Planetary Science Letters,* Vol. 403:
760 pp. 287-298. doi: 10.1016/j.epsl.2014.06.037.

761

762 Scala A., Festa G., & Vilotte J.-P. (2017). Rupture Dynamics Along Bimaterial Interfaces: a
763 Parametric Study of the Shear-Normal Traction Coupling. *Geophysical Journal International*,
764 209(1): 48-67. doi: 10.1093/gji/ggw489.

765

766 Shearer P. & Bürgmann R. (2010). Lessons Learned from the 2004 Sumatra-Andaman Megathrust
767 Rupture. *Annual Review of Earth and Planetary Sciences.* Vol. 38: pp. 103-131. doi:
768 10.1146/annurev-earth-040809-152537.

769

770 Shi B., Anooshehpoor A., Brune J. N., & Zeng Y. (1998). Dyanmics of Thrust Faulting: 2D Lattice
771 Model. *Bulletin of the Seismological Society of America*, Vol. 88, No. 6, pp. 1484-1494.

772

773 Takahashi N., Kodaira S., Tsuru T., Park, J.-O., Kaneda, Y., Suyehiro, K., Kinoshita H., Abe, S.,
774 Nishino, M. & Hino R., (2004) Seismic Structure and Seismogenesis Off Sanriku Region,

775 Northeastern Japan, *Geophysical Journal International*, Vol. 159, pp.129-145. doi: 10.1111/j.1365-
776 246X.2004.02350.x
777
778 Tanaka, H., Chen W. M., Wang, C. Y., Ma K. F., Urata N., Mori J., & Ando M. (2006). Frictional
779 Heat From Faulting of the 1999 Chi-Chi, Taiwan Earthquake. *Geophysical Research Letters* Vol. 33:
780 L16316. doi: 10.1029/2006GL026673.
781
782 Tanioka Y., & Satake K. (1996b). Fault Parameters of the 1896 Sanriku Tsunami Earthquake
783 Estimated from Tsunami Numerical Modeling. *Geophysical Research Letters* Vol. 23: pp. 1549-
784 1552. doi: 10.1029/96GL01479.
785
786 Thomas M. Y., & Bhat H. S., (2018). Dynamic Evolution of Off-Fault Medium During an
787 Earthquake: a Michromechanics Based Model. *Geophysical Journal International,* Vol. 214(2),
788 pp. 1267-1280. doi: 10.1093/gji/ggy129.
789
790 Uenishi K., & Rice J. R., (2003). Universal Nucleation Length for Slip-Weakening Rupture
791 Instability Under Nonuniform Fault Loading. *Journal of Geophysical Research,* Vol. 108(B1),
792 2042. doi:10.1029/2001JB001681.
793
794 Uenishi K., (2015). Dynamic Dip-Slip Fault Rupture in a Layered Geological Medium: Broken
795 Symmetry of Seismic Motion. *Engineering Failure Analysis,* Vol 58 (2), pp 380-393. doi:
796 10.1016/j.engfailanal.2015.07.004.
797
798 Vallage A., Klinger Y., Grandin R., Bhat H. S., & Pierrot-Deseilligny M., (2015). Inelastic Surface
799 Deformations During the 2013 $M_w$ 7.7 Balochistan, Pakistan, Earthquake. *Geology* Vol. 43(12): pp.
800 1079-1082. doi: 10.1130/G37290.1

Yue, H., Lay T., Li L., Yamazaki Y., Cheung K. F., Rivera L., Hill E. M., Sieh K., Kongko W., & Muhari A., (2015). Validation of Linearity Assumptions for Using Tsunami Waveforms in Joint Inversion of Kinematic Rupture Models: Application to the 2010 Mentawai Mw 7.8 Tsunami Earthquake, *Journal Geophysical Research: Solid Earth*, Vol 120, pp. 1728–1747, doi: 10.1002/2014JB011721.

Zhang, L., Wu, J. C., Ge, L. L., Ding, X. L., Chen, Y .L., (2008). Determining Fault Slip Distribution of the Chi-Chi Taiwan Earthquake with GPS and InSAR Data Using Triangular Dislocation Elements. *Journal of Geodynamics* Vol. 45(4-5): pp. 163–168. doi: 10.1016/j.jog.2007.10.003.

Zhou F., & Shioya T., (1996). Energy Balance Analysis on Mode-III Dynamic Crack Propagation in Fixed Sided Strip, *International Journal of Fracture,* Vol. 80: 33-44. doi:10.1007/BF00036478.